

## Creation and annihilation of reflection shift vortices on the interface between multifold Weyl semimetals

Qiao He , Rui-Qiang Wang, Ming-Xun Deng, and Mou Yang <sup>\*</sup>

*Guangdong Basic Research Center of Excellence for Structure and Fundamental Interactions of Matter, Guangdong Provincial Key Laboratory of Quantum Engineering and Quantum Materials, School of Physics, South China Normal University, Guangzhou 510006, China*



(Received 16 November 2023; revised 7 December 2023; accepted 10 January 2024; published 29 January 2024)

When an electron beam hits an interface at a point, the reflection beam comes back from another interface point and a reflection shift occurs in real space. We investigate the reflection shift evolution and Fermi arcs on the interface between two Multifold Weyl semimetals by changing the system parameters continuously using tight-binding calculations. The incident pocket is touched tangentially by Fermi arcs through reflection shift vortices located on the pocket edge. When the transmissive pocket is changed by tuning the parameters of the transmissive side, the edge vortex is shifted to inner locations by the transmissive pocket covering it. In the intersection region between the two pockets, the vortex and antivortex pair can be created and annihilated. The net number of vortices in the incident pocket for any case and that in the transmissive pocket if the reflection shift can be defined there, are just the monopole topological charges of the incident and transmissive media, respectively. Our work uncovers new quantized features of interfaces between topological materials.

DOI: [10.1103/PhysRevB.109.035434](https://doi.org/10.1103/PhysRevB.109.035434)

### I. INTRODUCTION

When a light beam is reflected by a flat interface, the reflected and incident beams do not meet at the same point on the interface and the reflection experiences an anomalous shift [1]. The longitudinal component of the displacement is known as Goos-Hänchen (GH) shift and the transverse component is named Imbert-Fedorov (IF) shift. Since the wave-particle duality holds for any particle and because the analogy between the energy dispersion of photons and that of quasiparticles in Weyl semimetals, the reflection shift effect may also be found in electronic systems of condensed matters [2].

The Weyl semimetal [3–10], the electron and valance bands of which are degenerate at points in momentum space called Weyl points and the energy dispersion near Weyl points is linear, has drawn much attention of physical society in recent years. Weyl points come in pairs, and the two Weyl points in one pair are the source and sink of the Berry curvature. The Berry curvature flux around a Weyl point over  $2\pi$  defines the Chern number associated with the Weyl point and also can be viewed as the topological charge in momentum space. In a typical Weyl material, a Weyl point carries a unit topological charge (positive or negative) and so a Weyl point pair is a dipole of topological charge in momentum space. The property of chirality of Weyl point leads to chiral anomaly [6–10], which is the physical origin of many transport effects such as planar Hall effect and 3D Hall effect [8, 10–12]. The chiral anomaly also leads to the appearance of topologically protected Fermi arcs that consist of localized states on the Weyl material surfaces [8–10, 13]. On the junction of two

different Weyl semimetals, the junction interface is a common surface of two beside materials, and the Fermi arcs of individual materials interact and lead to the reconstruction of Fermi arcs on the interface [14–18]. The interface Fermi arcs are expected to exhibit unique transport signals [19–21], and high quality interfaces between Weyl semimetals can be realized experimentally [22]. In addition to the usual Weyl semimetals exhibiting linear dispersion, multifold Weyl semimetals [23–25], of which a Weyl point carries one more topological charge ( $N > 1$ ), have a mix of linear and higher-order dispersions, and Weyl semimetals with  $N = 2, 3$ , and 4 were reported [24–27]. Due to the fantastic properties of Weyl semimetals, the interest in Weyl quasiparticles in crystal solid is extended to that in metamaterials such as cold atoms [28], resonator lattices [29], photonic crystals [30–33], and phononic crystals [34, 35].

The reflection shift of electron beam in Dirac-like materials was first noticed in graphene systems [36]. Because graphene is a pure 2D material, only the GH shift can happen. Weyl semimetals, as 3D cousins of graphene, are expected having the similar beam shift effect as in graphene. Following, it was found that not only the reflected beam is displaced at Weyl interfaces, the transmission beam is shifted too [37], while the reflected shift is much notable than the transmissive one. The IF component of reflection shift at potential step interfaces in Weyl semimetals [38–40], as well as the interfaces between normal and superconducting materials [41], stems from the angular momentum conservation when reflection and is proportional to the topological charge of the Weyl point, while the GH component cannot be explained by this conservation law. The reflection shift has its geometric origin [42], and it needs a correction beyond the linear approximation to remove the divergency at critical incident angles

<sup>\*</sup>yang.mou@hotmail.com

[43]. When electrons are injected from a Weyl medium to vacuum, there are semivortex structures of reflection shift locating where the Fermi arc states transit to bulk states in momentum space [44,45]. At the interface between two Weyl media with mismatched Weyl dipoles, interface Fermi arcs are constructed, and semivortices can also be found at the joint points between the incident bulk states and the interface Fermi arc states [46]. If electrons are injected from a normal metal to a Weyl medium, full vortices, not semivortices, are found and a vortex means a quantized circulation [47]. The circulation stems from the winding of the complex phase of reflection coefficient, and such a reflection phase can be detected in metamaterials [48–51].

However, what the physical connection between semivortices and full vortices is and which side medium, incident or transmissive side, is responsible for the number of these vortices, are still unclear. Motivated by these questions, we calculate the reflection shift and the density of states (DOS) on the interface between two different multifold Weyl semimetals. The incident energy defines an incident pocket and a transmissive pocket. Vortices of the reflection shift and Fermi arcs on the interface are found respectively in the incident pocket and outside it. Every vortex on the incident pocket edge (semivortex) is planted with a Fermi arc while the vortex in the inner region (full-vortex) is not. At the centers of inner vortices, the transmission reaches unit perfectly. The parameters of the transmissive side medium are tuned to continuously change the position and size of transmissive pocket. If the transmissive pocket overlaps an edge vortex, the edge vortex is detached with the pocket edge to become an inner one, saying, the semivortex becomes a full vortex. Vortex pair with opposite helices can be generated and annihilated in the overlap region, so the total number of vortices is changed but the net number of vortices is conserved, which is the topological charge of the incident Weyl medium. When the incident pocket includes the transmissive one, which means the reflection shift can be defined in the whole transmissive pocket, the number of vortices appearing in the transmissive pocket is the monopole topological charge of the transmissive medium.

To obtain the reflection coefficient of the multifold Weyl junction as well as the DOS on the interface, we develop a tight-binding method based on the lattice description of the junction. Our method not only can be applied for the Weyl junctions, but also can be used to solve transport problems of other systems with more complicated geometry.

This paper is organized as follows. In Sec. II, we describe the model of multifold Weyl media and the Weyl junction we considered. In Sec. III, we briefly introduce the calculation method of reflection shift and interface DOS. In Sec. IV, we investigate the evolution of the reflection shift vortices and the interface DOS by changing the parameters of the transmissive side continuously. In Sec. V, we summarize our main conclusions. The lattice description of the multifold Weyl junction and the calculation details are presented in Appendix.

## II. MULTIFOLD WEYL JUNCTION

The heterojunction is constructed by jointing two different multifold Weyl materials. The low-energy Hamiltonian of the

multifold Weyl material for each side is modeled by

$$H = \begin{bmatrix} q_z + U & (q_x - i\chi q_y)^N \\ (q_x + i\chi q_y)^N & -q_z + U \end{bmatrix} \quad (1)$$

and the corresponding bulk band energies are

$$E = U \pm \sqrt{(q_x^2 + q_y^2)^N + q_z^2}, \quad (2)$$

where  $q_x = 2 + \cos k_w - \cos k_x - \cos k_y - \cos k_z$ ,  $q_y = \sin k_y$ ,  $q_z = \sin k_z$  with  $k_\alpha$  ( $\alpha = x, y, z$ ) being the wave vector component in  $\alpha$  direction and  $k_w$  being the half of Weyl point connection length,  $N$  is the topological charge number of Weyl points,  $U$  is the potential to lift the energy, and  $\chi = \pm 1$  indicates the chirality of the Hamiltonian. Equation (1) describes the multifold Weyl semimetal with one pair of  $N$ -fold Weyl points locating at  $(\pm k_w, 0, 0)$  in  $k$  space. The junction interface lies along the plane of  $z = 0$ , and the Hamiltonian parameters  $N$ ,  $U$ ,  $\chi$  and  $k_w$  in the region  $z < 0$  and those in the region  $z > 0$  can be all different. We use the subscript 1 to the label quantities for  $z < 0$  and adopt the subscript 2 to denote them for  $z > 0$ . For example, the lift potential for  $z < 0$  is assumed to be zero but that in the region of  $z > 0$  is set to be  $V$ , saying,  $U_1 = 0$  and  $U_2 = V$ . In low-energy limit, the dispersion near each Weyl point is linear along  $k_z$  axis and proportional to  $k^N$  in other two principal directions. The layout of the Weyl junction and the reflection shift are illustrated in Fig. 1(a), and the dispersions of two beside media along  $k_x$  direction are sketchily shown in Fig. 1(b). The calculations in the following sections are based on the tight-binding version of the Hamiltonian. How to construct the tight-binding Hamiltonian according to Eq. (1) is not presented here but is given in Appendix A.

The electrons to be considered are those near the Weyl points  $(k_w, 0, 0)$  and to be injected from the region of  $z < 0$  to that of  $z > 0$ . We refer the  $k_x$ - $k_y$  plane projection of the equienergy surface of the incident medium as the incident pocket and name that of transmissive material as the transmissive pocket. An injected or transmitted state of energy  $E$  can be represented by a point in the incident or transmissive pocket, respectively. Because of the translational invariance in  $x$  and  $y$  directions, the injected and transmitted states possess the same in-plane wave vector. If an injected state in the incident pocket also falls in the transmissive pocket, the state has probability to be transmitted to a propagating state in the transmissive side, otherwise, it is totally reflected back. Figure 1(c) schematically shows a possible configuration for the incident and transmissive pockets.

## III. REFLECTION SHIFT AND DENSITY OF INTERFACE STATES

When a beam of Weyl fermions is injected onto the junction interface, it hits on the interface at a point. The reflected beam and transmitted one stem from other two points on the interface, saying, the reflection point and transmission point. The reflection shift  $\mathbf{S}$ , which is defined by the vector originated from the injection point and ended at the reflection point, is calculated by [42]

$$\mathbf{S} = \mathbf{A}_r - \mathbf{A}_i - \nabla \arg r, \quad (3)$$

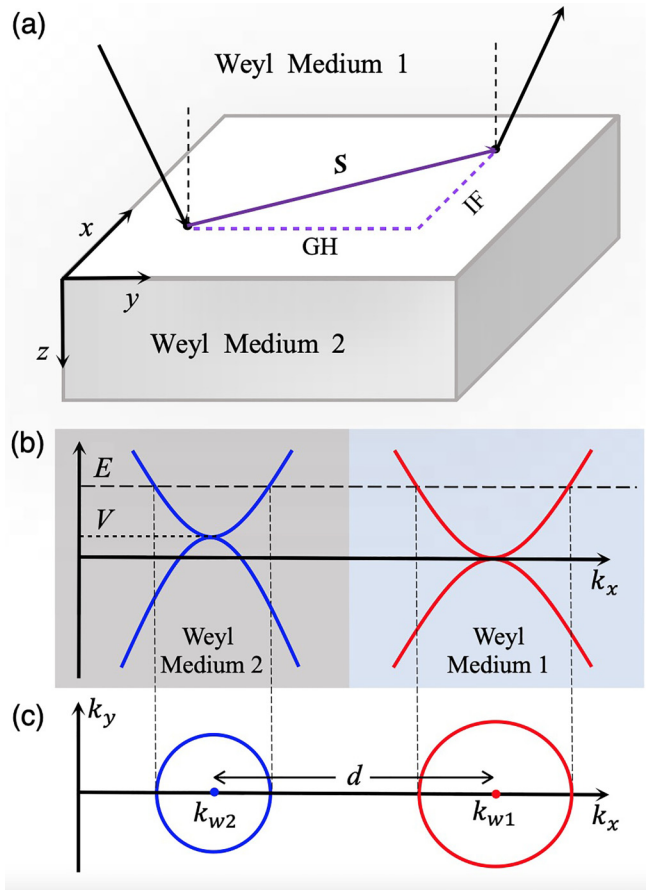


FIG. 1. (a) A reflection shift takes place when a beam of Weyl fermions is injected from medium 1 to medium 2. (b) Energy dispersions of multifold Weyl materials beside the interface in  $k_x$  direction. (c) The incident and transmissive pockets (red and blue loops) in  $k_x-k_y$  plane.

where  $A_\alpha = i\langle\phi_\alpha|\nabla|\phi_\alpha\rangle$  ( $\alpha = i, r$ ) are the in-plane Berry connection for the incident state  $|\phi_i\rangle$  and that for the reflected state  $|\phi_r\rangle$ ,  $r$  is the reflection coefficient (It is associated with the reflected state as  $r|\phi_r\rangle$ ) and  $\nabla$  stands for the gradient operator in  $k_x-k_y$  plane. In the equation, the first two terms rely only on intrinsic band geometric property of the incident side, while the last term depends on band structures of both sides. The reflection coefficient is a function of  $k_x$  and  $k_y$  at a fix energy, saying  $r = r(k_x, k_y)$ , and it is numerically calculated point by point in  $k_x-k_y$  plane using the method described in Appendix B based on the tight-binding version of the Hamiltonian in Eq. (1). The transmission probability  $1 - |r|^2$  is also calculated to identify the inner vortices.

The Berry connections in Eq. (3) serve as the compensation source for gauge changing since the reflection coefficient is gauge dependent. If we adopt another gauge so that the reflected state is  $|\phi'_r\rangle = |e^{-if_r}\phi_r\rangle$ , where  $f_r$  is a function of  $k_x$  and  $k_y$ , we have  $r|\phi_r\rangle = re^{if_r}|\phi'_r\rangle = r'|\phi'_r\rangle$  with  $r' = re^{if_r}$ , and  $\nabla \arg r' = \nabla \arg r + \nabla f_r$ . Meanwhile, the Berry connection of the new reflected state turns to be  $A'_r = i\langle\phi'_r|\nabla|\phi'_r\rangle = A_r + \nabla f_r$ . Apparently, the change effect of reflection coefficient is canceled by that of Berry connections in the reflection shift.

It is well known that there exist surface states on the junction interface. These states locate near the interface and decay

into the bulk. The interface DOS reveals the Fermi arcs on the interface if they exist. The interface Fermi arcs are sensitive to the Hamiltonian parameters of two sides and have relation with the reflection shift in  $k_x-k_y$  space. The interface DOS is defined by

$$\text{DOS} = \frac{i}{2\pi} \text{Tr}(G - G^+), \quad (4)$$

where  $G$  is the retarded Green's function of the interface region. Our calculation of the retarded Green's function is also based on the tight-binding model, and the calculation details are presented in Appendix C.

#### IV. VORTICES OF REFLECTION SHIFT AND FERMION ARCS ON INTERFACE

On the interface between single fold Weyl materials, it was reported that the incident and the transmissive pockets are connected tangentially by an interface Fermi arc [44,46]. For each incident state in the incident pocket, its reflection shift can be calculated, so the distribution profile of reflection shift can be obtained. At the tangent point between the incident pocket and Fermi arc, there exists a vortex of reflection shift. When we turn to the multifold Weyl junction, it is expected that there are more Fermi arcs on the interface and more vortices on the incident pocket edge arise. Moreover, the difference of the topological properties in two sides, explicit saying, the topological charges and chiralities, could introduce interesting features of the reflection shift vortices and interface Fermi arcs.

In this section, we will investigate the reflection shift vortices and interface Fermi arcs of the multifold Weyl junction with different topological charge numbers besides, specifically saying,  $N_1 = 3$  and  $N_2 = 2$  will be adopted in the following calculations. We fix the incident pocket by setting  $E = 0.025$  and  $k_{w1} = \pi/2$ , and let the transmissive pocket change by tuning the parameters of transmissive side to observe the evolution of the vortices and Fermi arcs on the interface. Explicitly, the changeable parameters of transmissive side are  $V$  and  $k_{w2} = k_{w1} + d$ , where  $d$  is the Weyl point mismatch.

##### A. Interface of same chirality configuration

The chiralities of the beside Weyl materials are set to be  $\chi_1 = 1$  and  $\chi_2 = 1$ . The transmissive pocket is initiated on the left to the incident pocket without interacting with it, as shown in Fig. 2(a). The reflection shift is indicated by arrows. The Fermi arcs are revealed by the interface DOS that is visualized by the shading (darker means larger) outside the incident pocket. The incident pocket, in which a triple Weyl point is included, spins three Fermi arcs, and the transmissive pocket, which is a double Weyl one, is touched by two Fermi arcs. These Fermi arcs can be categorized into two types, those bridge the pockets belong to the same side material (named as surface arcs in the following) and those connect the pockets of different side materials (named as interface arcs). The pair of red loops in the inset are pockets of incident medium, and the pair of blue loops are those of transmissive medium. Around the incident pocket, there is one interface arc, which is accepted by the transmissive pocket, and two surface arcs

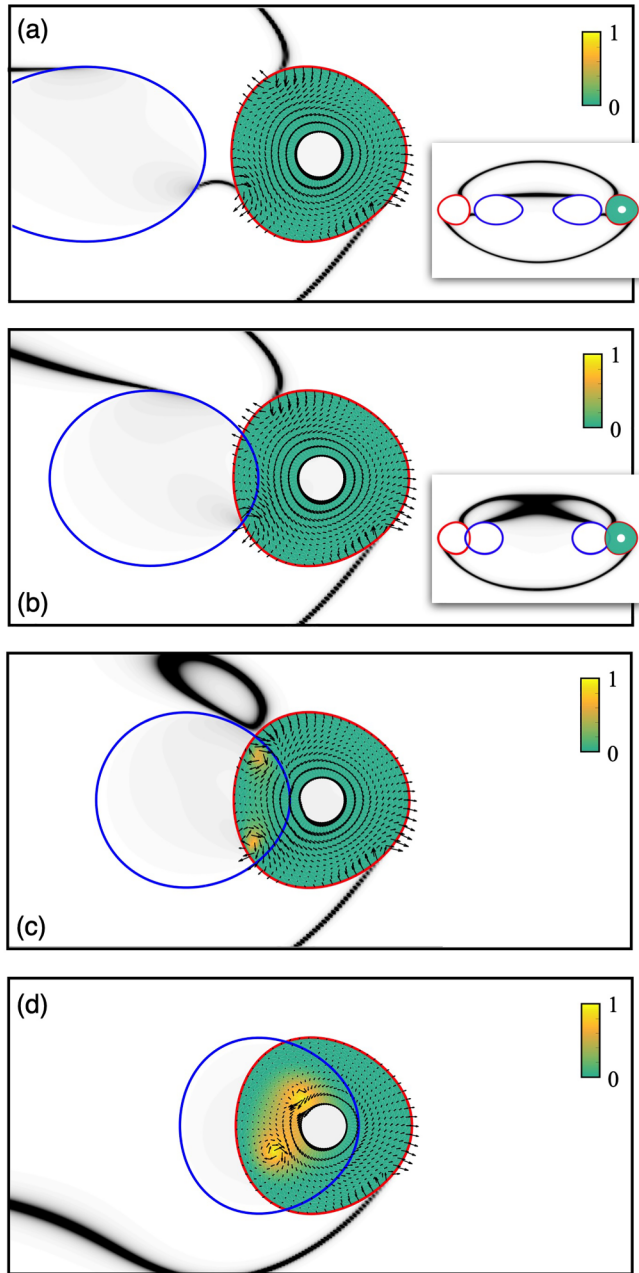


FIG. 2. Evolution of the Fermi arcs on interface and the reflection shift vortices in  $k_x-k_y$  space for the same chirality configuration when the incident pocket (red loop) is fixed and the transmissive pocket (blue loop) changes. The color in the incident pocket indicates the transmission probability. The insets show the full view of Fermi arc profiles. The Weyl point mismatch  $d$  takes values  $-2.5$ ,  $-1.8$ ,  $-1.4$ , and  $-0.6$  in (a) through (d), respectively (in units of average radius of the incident pocket). The potential in the transmissive side  $V = -0.06$  in all panels.

can be found that are recycled by the other pocket of the incident medium. The states of the surface and interface arcs are both localized near the same interface. All Fermi arcs are connected to pockets tangentially, which reflects the transition between localized interface state and bulk state. The number of Fermi arcs connecting to a pocket is just the number of its topological charge, saying, three and two for the incident and

transmissive pockets respectively. At the touch points between incident pocket and Fermi arcs, reflection shift vortices with same helix can be found. Because the vortex centers locate exactly on the pocket edge and the reflection shift can only be defined in the incident pocket, only half-vortices are left and visible. The edge vortices can be viewed as spinneret orifices spinning out silk of Fermi arcs. These Fermi arcs cannot be dangling outside and have to run for being wrapped on another pocket.

We tune the parameter  $k_{w2}$  to move the transmissive packet rightward. At the beginning, a surface arc of the transmissive pocket and a surface one of the incident pocket attract each other. The two attracted surface arcs will touch and evolve into interface arcs if the incident and transmissive pockets become closer. Because the interface arc (the shortest arc in the above figure) is shortened, at a certain distance between the two pockets after they intersect, the length of the interface arc decreases to zero, so its spinneret orifice on the incident pocket touches its reception spot on the transmissive pocket. The situation is demonstrated as Fig. 2(b).

The intersection region is enlarged when the transmissive pocket moves on. In the intersection region, nonzero transmission occurs. The newly formed interface arc is retracted and the spinneret orifice closest to the transmitted pocket (the left most one in the above figure) is covered by the intersection region, its Fermi arc is directly absorbed by the transmissive pocket without being spun out since no interface state is physically allowed in the transmissive pocket. The vortex of spinneret orifice is driven away from the edge to drift into inner region in the incident pocket and the full vortex structure is exposed. Following, the intersection region overlaps the second edge vortex, which is the spinneret orifice of the newly formed interface arc, the edge vortex is pushed into the inner region to become a full vortex too. The centers of the full vortices locate at the positions where the transmission probability is exactly unit, which is revealed by the hot spots in the intersection region. Because the second spinneret orifice disappears, the new interface arc loses its joint points on both pockets. The interface arc is detached away and becomes an isolated Fermi ring [16–18], as shown in Fig. 2(c).

When the transmissive pocket continues to move in, the two vortices in the intersection region swim far away from the edge into the deep, and Fermi ring shrinks and then fades out. The last Fermi arc of the incident packet, which is a surface one, accompanied with its edge vortex, is left along, as Fig. 2(d) shows.

The Weyl point of the transmissive side has to encounter that of the incident side if the transmissive pocket moving continues. In the special case, the incident and transmissive pockets are almost overlap. To observe what happens in the gap between the incident and transmissive pockets, at the mean time of moving the transmissive pocket, we change the lift potential in the transmissive side to adjust its pocket size. We tune the potential so as to reach two different situations between the two packets. First, the transmissive pocket is the larger one and includes the incident packet completely. Second, the transmissive pocket is the smaller one and is surrounded by the incident packet totally.

From Fig. 3(a) on [it is identical to Fig. 2(d), we duplicate it to guide eyes more friendly], when the transmissive pocket

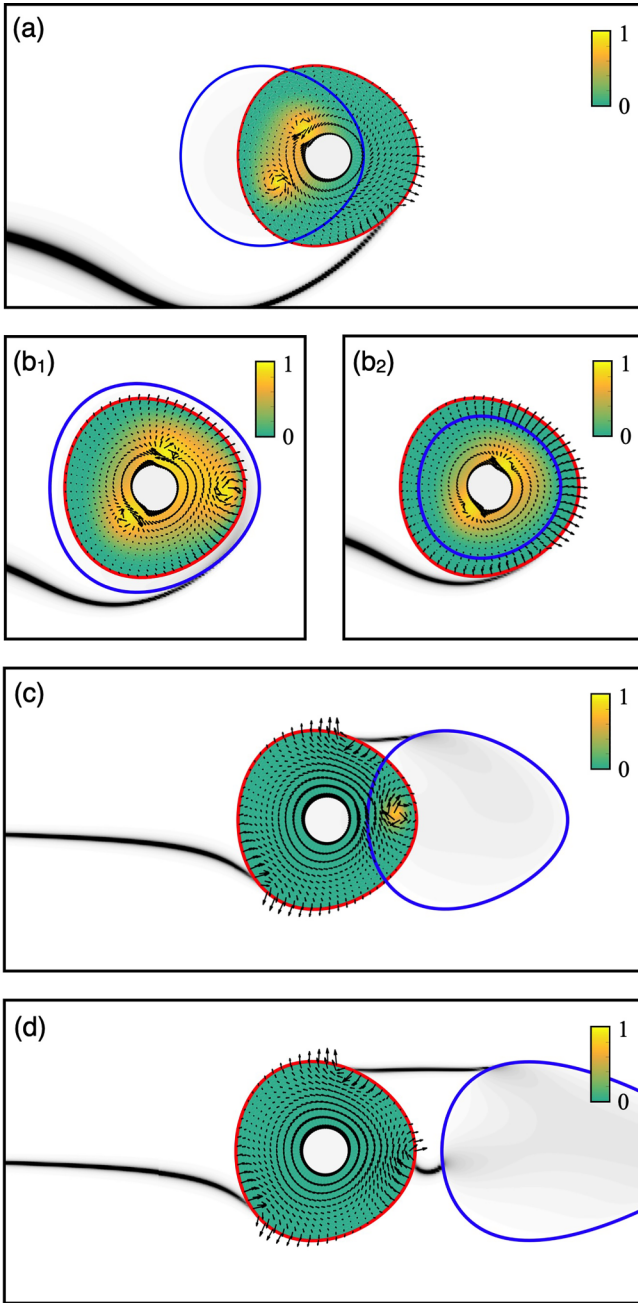


FIG. 3. Evolution of the Fermi arcs on interface and the reflection shift vortices in  $k_x-k_y$  space for the same chirality configuration. The Weyl point mismatch  $d = -0.6, 0, 1.5, \text{ and } 2.5$  in (a) through (d) respectively, and the potential  $V = -0.06$  in all panels except that  $V = -0.09$  and in (b<sub>1</sub>) and  $V = -0.03$  in (b<sub>2</sub>).

shifts and expands to include the incident pocket, the last spinneret orifice is covered by the transmissive pocket, the incident pocket loses its last surface Fermi arc that does not disappear but is taken over by the transmissive pocket smoothly, and the last edge vortex goes down into the pool of intersection. All the spinneret orifices disappear and they are transformed into inner vortices. Figure 3(b<sub>1</sub>) illustrates the situation. We restore transmissive pocket to its normal size after it passes the incident pocket. The transmitted pocket leaves the incident one gradually, the intersection region becomes smaller and

smaller. The inner vortices swim back to the bank one by one and will be settled on the incident pocket edge to recover their role of spinneret orifices. Every time a spinneret orifice is released by the transmissive pocket, a Fermi arc is spun and a surface or an interface arc is restored, as shown in Figs. 3(c) and 3(d).

If the transmissive pocket shrinks into the incident one as shown in Fig. 3(b<sub>2</sub>), it cannot include the last edge vortex and the attached surface arc are always kept. The two contained vortices are drawn to deeper region. Now one edge vortex is left, two inner vortices drift near the incident pocket center, and the total number of vortices is still three. When the transmissive pocket restores its usual size and leaves, the two vortices swim back and the corresponding interface arcs are recovered one by one. The procedure is demonstrated in Figs. 3(c) and 3(d).

In the process that transmissive pocket changes, the surface and interface arcs can be transit through and back. The Fermi arcs on the incident pocket can be erased by the covering of the transmissive pocket on the spinneret orifices. No Fermi arc is connected to the incident pocket when it is totally included the transmissive one, and it possesses  $N_1 - N_2$  Fermi arcs if it included the transmissive pocket. The edge vortices can be extruded from the incident pocket edge to inner positions where the perfect transmission takes place. Though the number of edge vortices can be eliminated by the transmissive pocket covering, the total number of vortices (it will be updated as net number for more general cases in the following section), edge vortices and inner ones, is always  $N_1$ , the topological charge of the incident medium, and it can be viewed as a conserved quantity. The figures described in this subsection are only few snapshots of the process that the incident pocket moves from left to right. The dynamic pictures to show the evolution of the reflection shift and interface DOS in the process are provided in the Supplemental Material [52].

### B. Interface of opposite chirality configuration

We set the Hamiltonian chiralities of the Weyl beside materials as  $\chi_1 = 1$  and  $\chi_2 = -1$ . The transmissive pocket is initialed as shown in Fig. 4(a). It is placed left to the incident pocket at the same location as in the same chirality case, and the two cases share some similar features. There are three Fermi arcs joining to the incident pocket at edge vortices with same helix and two Fermi arcs connect to the transmissive pocket. Unlike in the same chirality case, the Fermi arcs spun by the incident pocket, none of which is ended on the transmissive pocket, are all surface arcs. We catalyze these surface arcs into two types, the incident arcs that connect the pockets of the incident medium, and the transmissive arcs that bridge the pockets for transmissive side (see the inset).

We increase the parameter  $k_{w2}$  to move transmissive packet rightwards. After the transmissive pocket intersects with the incident one, in the intersection region, a hotspot area of high transmission bubbles out, in which the reflection shift orientation is changed apparently, as shown in Fig. 4(b). The hotspot area expands in the next and a pair of vortices with opposite helices are created there. At the centers of the two opposite vortices, the transmission probability reaches unit. Figure 4(c) shows the situation.

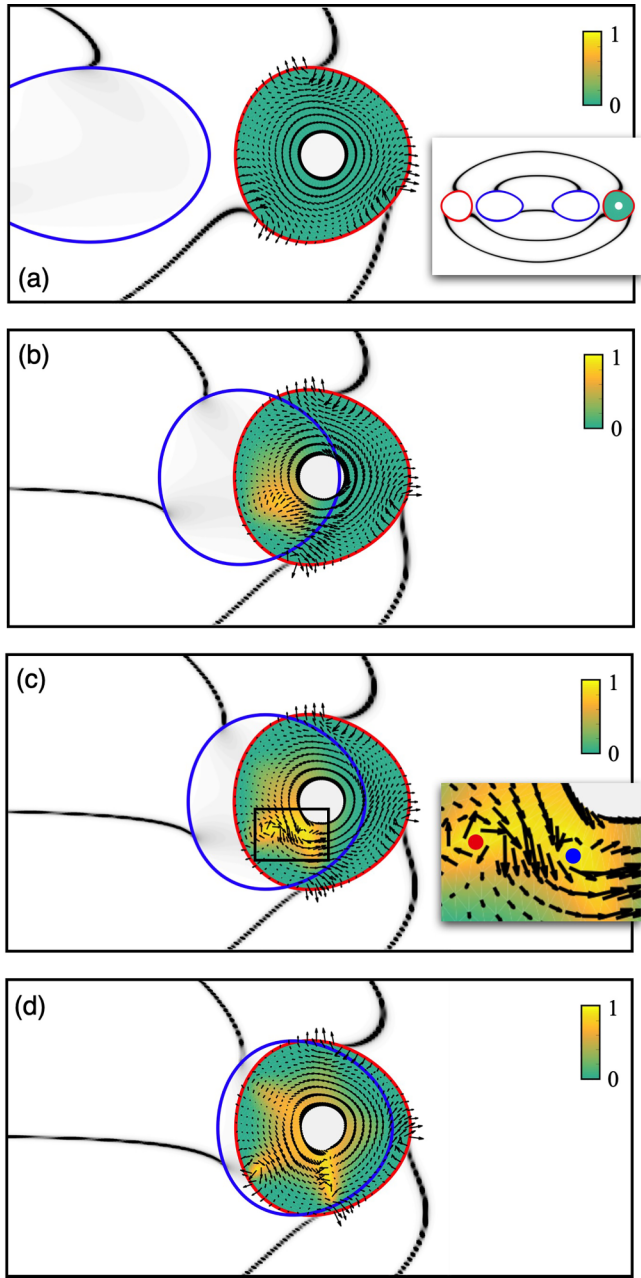


FIG. 4. Evolution of Fermi arcs on interface and reflection shift vortices in  $k_x-k_y$  space for opposite chirality configuration. The inset in (a) shows the full view of Fermi arc profiles and the inset in (c) is the zoom view of the vortex (red bold dot) and antivortex (blue bold dot) pair. The Weyl point mismatch  $d = -2.5, -0.8, -0.5,$  and  $-0.2$  in (a) through (d) respectively and the potential  $V = -0.06$  in all panels.

The pair of newly generated vortices are driven to drift separately in different directions. One of the vortices, that has opposite helix with respect to the edge vortices (referred as antivortex), runs downward to the edge vortex which is the nearest one to the transmissive pocket, and the other moves in lower-left direction, as Fig. 4(d) shows.

As before, we change the lift potential of the transmissive medium to adjust the pocket size when the two pockets nearly overlap. First, we set the transmissive packet to be the larger

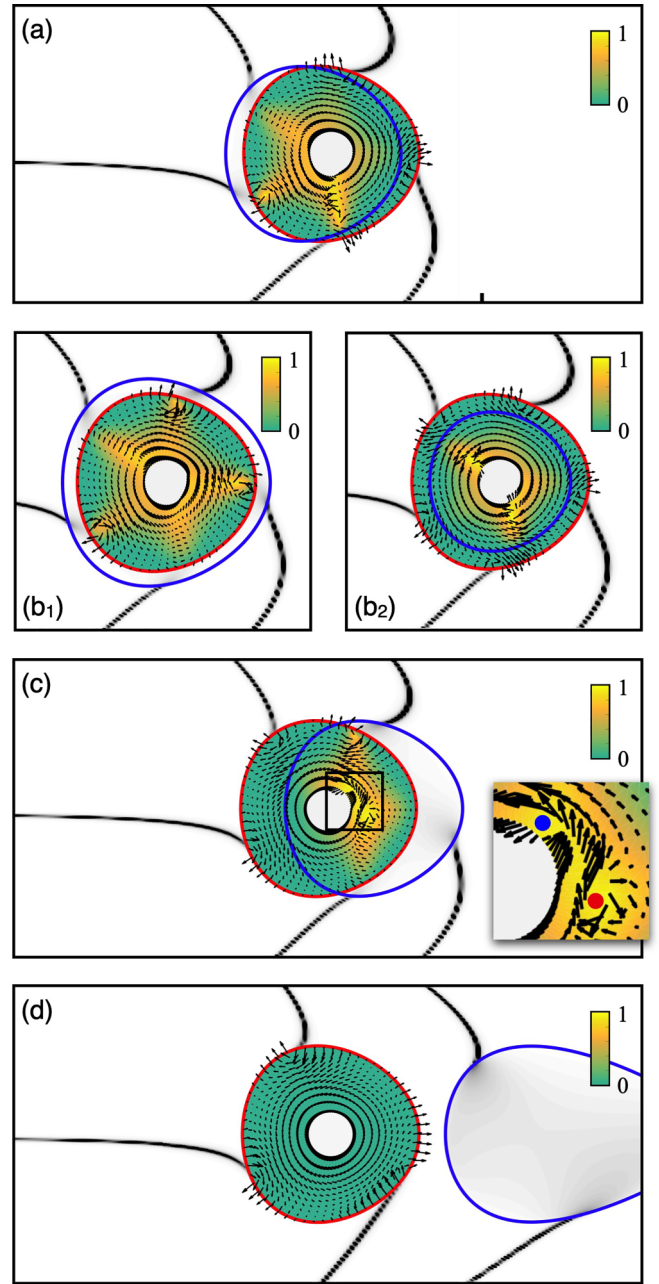


FIG. 5. Evolution of Fermi arcs on interface and reflection shift vortices in  $k_x-k_y$  space for the opposite chirality configuration. The inset in (c) is the zoom view of the vortex and antivortex pair. The Weyl point mismatch  $d = -0.2, 0, 0.5,$  and  $2.5$  in (a) through (d) respectively, and the potential  $V = -0.06$  in all panels except that  $V = -0.09$  (b<sub>1</sub>) and  $-0.03$  (b<sub>2</sub>).

one. If transmissive packet moves and expands from the situation shown in Fig. 5(a), which is same as Fig. 4(d) to guide eyes, the transmissive pocket covers the nearest edge vortex (the lowest one), the edge vortex is firstly detached from the edge into the inner region, and immediately encounters the antivortex running for it and is canceled out by the merging of opposite helices, so the corresponding incident arc loses its landing point and is transited onto the transmissive pocket. The covering of the spinneret orifice by the intersection region does not lead to the disappearance of Fermi arc, but results

in the transition from incident arc to transmissive one. The other vortex in the created vortex pair, which possesses the same helix as the edge vortices have, hovers near left bottom of incident pocket. When the transmissive packet includes the incident one completely as shown in Fig. 5(b<sub>1</sub>), the remained two incident arcs are taken over by the transmissive pocket and their edge vortices are pushed away from the edge to become inner vortices. Therefore five Fermi arcs, two of which are transmissive arcs and three of which are initially belong to the incident pocket, are all carried by the transmissive pocket.

Second, we set the transmissive packet to be the smaller one and move it to the incident pocket from the situation of Fig. 5(a). The antivortex in the created pair retreats back, and the other vortex is anchored on the incident pocket edge as an edge vortex to receive a transmissive arc (the left-most one) that is belong to the transmissive pocket and the antivortex is left in the pool. When the transmissive pocket is surrounded by the incident one, the last transmissive arc (the upper-left one) is transited onto the incident pocket. To settle the last transmissive arc, a new edge vortex is needed. To achieve this, a vortex and antivortex pair has to be generated before, the normal vortex in the vortex pair runs to the incident pocket edge, and remained one, another antivortex, is thrown in the pool. Now the incident pocket has five spinneret orifices and spins five Fermi arcs, and two antivortices are left near the incident pocket center. This situation is demonstrated in Fig. 5(b<sub>2</sub>).

When the transmissive pocket moves out, the intersection region shrinks. The incident and transmissive pockets take back their own Fermi arcs gradually. Before the intersection region vanishes, the pair of vortices with opposite helices are left behind in the residual hotspot area, as a vortex and antivortex pair arises when intersection region begins to be enlarged previously. The vortex pair will be canceled out later by merging together. Finally, the transmissive pocket is decoupled with the incident one, and all the Fermi arcs come back to their home pockets, as indicated in Figs. 5(c) and 5(d).

For the opposite chirality configuration, the maximum number of spinneret orifices on the incident pocket edge  $N_1 + N_2$  (the incident pocket surrounds the transmissive one) and the minimum number is zero (the incident pocket is included by the transmissive one). The vortices can be created and annihilated pairwise, so the total number of vortices varies, while the net number of vortices is conserved as its initial value  $N_1$ . The dynamic pictures to show the whole process of the incident pocket moving are presented in the Supplemental Material [52].

## V. CONCLUSION AND SUMMARY

We presented a systematic study of the reflection shift and surface states between two multifold Weyl semimetals. There are Fermi arcs, states of which are localized near the junction interface, connect the pockets of incident and/or transmissive media. Reflection shift vortices are found in the incident pocket and the vortices on the pocket edge work as spinneret orifices of Fermi arcs. The covering of edge vortices by the transmissive pocket shifts the vortices from the edge to inner regions where the perfect transmissive takes place. Vortices

can be created and annihilated in positive-negative helices pairs in the intersection region between the incident and transmissive pockets, so the number of vortices is changeable but the net number is a conserved quantity, that is  $N_{\text{net}} = \chi_1 N_1$  (In this paper,  $\chi_1 = 1$  is the default choice). At the centers of a pair of vortex and antivortex, the transmission probability reaches unit also. In other words, whatever the origination of an inner vortex is, an edge vortex slipping into the pool or a vortex (normal vortex or antivortex in a vortex pair created), the perfect transmission at its location is always true.

The cases of the incident pocket including the transmission one are most important to reflect the topological properties of the junction interface because if so the reflection shift is well defined not only in the incident pocket but also in the whole transmissive pocket. The number of edge vortices as well as the number of Fermi arcs carried by the incident pocket is  $N_{\text{edg}} = \chi_1 N_1 - \chi_2 N_2$ . To ensure the net number  $N_{\text{net}}$  be an unchanged quantity, we must have  $N_{\text{inn}} = N_{\text{net}} - N_{\text{edg}} = \chi_2 N_2$  pieces of inner vortices appearing in the intersection region (also the transmissive pocket region). In our examples of the two configurations,  $N_1 = 3$  and  $N_2 = 2$  are used. For the same chirality configuration, we have  $N_{\text{net}} = 3$ ,  $N_{\text{edg}} = 1$ , and  $N_{\text{inn}} = 2$  that means 2 inner vortices inside. For the opposite chirality configuration, we have  $N_{\text{net}} = 3$  and  $N_{\text{edg}} = 5$ , therefore  $N_{\text{inn}} = -2$  that means 2 antivortices appearing in the transmissive pocket. Though the vortex pair creation and annihilation are not observed in the same chirality configuration, indeed they can occur in other examples not shown in this paper. For instance, if we set  $N_1 = 2$  and  $N_2 = 3$ , we will have edge vortex number  $N_{\text{edg}} = 2 - 3 = -1$ , which means there is an antivortex landing on the incident pocket edge and the antivortex must be generated by the vortex pair creation.

The reflection coefficient is a function of every parameter of both sides. However, the net number of vortices is only determined by the topological charge of the incident medium for any configurations between incident and transmissive pockets. In case the reflection shift in the transmissive pocket can be well defined, the net number of vortices in the transmission pocket only depends on the topological charge of the transmissive medium. Our work uncovers new topological features of interfaces between Weyl media and will lead to a further understanding of the nature of the topological phase of matters.

## ACKNOWLEDGMENTS

This work was supported by the National Natural Science Foundation of China under Grants No. 12174121 and No. 12274146 and the Guangdong Basic and Applied Basic Research Foundation under Grant No. 2023B1515020050.

## APPENDIX A: TIGHT-BINDING MODEL OF THE WEYL JUNCTION SYSTEM

The Weyl Hamiltonian in Eq. (1) can be rewritten as

$$H = U + q_z \sigma_z + (q_x - i\chi q_y)^N \sigma_+ + \text{H.c.}, \quad (\text{A1})$$

where  $\sigma_\alpha$  ( $\alpha = x, y, z$ ) are the  $\alpha$ -component Pauli matrices and  $\sigma_\pm = (\sigma_x \pm i\sigma_y)/2$ . We preserve  $k_x$  and  $k_y$  as good quantum

numbers and discretize the Hamiltonian in  $z$  direction on a 1D chain with unit lattice constant.

To express the tight-binding Hamiltonian conveniently, we define an generator matrix of infinite dimension on the 1D lattice,

$$K = \begin{pmatrix} \ddots & & & & & \\ & \ddots & & & & \\ & & 0 & 1 & & \\ & & & 0 & 1 & \\ & & & & 0 & \ddots \\ & & & & & \ddots \end{pmatrix}. \quad (\text{A2})$$

Using the matrix,  $\cos k_z$  and  $\sin k_z$  in the Hamiltonian (They are included in  $q_x$ ,  $q_y$ , and  $q_z$ ) are translated into

$$\begin{aligned} \cos k_z &= 1 - \frac{1}{2}(K + K^+) = 1 - P_+, \\ \sin k_z &= \frac{1}{2i}(K - K^+) = P_-, \end{aligned} \quad (\text{A3})$$

where  $P_+ = (K + K^+)/2$  and  $P_- = (K - K^+)/2i$  are two Hermitian matrices. The term  $(q_x + i\chi q_y)^N$  in the Hamiltonian is a polynomial of  $P_+$  with the highest power  $N$ . We know  $P_+$  leads to nearest hopping, so  $P_+^2$  produces next-nearest hopping,  $P_+^3$  results in next-next-nearest hopping, and  $P_+^N$  brings about the  $N$ 'th nearest hopping. Recalling the expressions of  $q_x$ ,  $q_y$ , and  $q_z$ , the Hamiltonian matrix of the tight-binding model is

$$H = U + \sigma_z P_- + [\sigma_+(M + P_+)^N + \text{H.c.}] \quad (\text{A4})$$

with  $M = 1 + \cos k_w - \cos k_x - \cos k_y - i\chi \sin k_y$ .

We demonstrate how to construct the tight-binding model by assuming the Hamiltonian has next nearest hopping, that means  $N = 2$ . Generally saying, the translational symmetric Hamiltonian with next nearest hopping has the form

$$H = \begin{pmatrix} \ddots & & & & & \\ \ddots & H_{11} & H_{12} & H_{13} & & \\ \ddots & H_{12}^+ & H_{11} & H_{12} & H_{13} & \\ & H_{13}^+ & H_{12}^+ & H_{11} & H_{12} & \ddots \\ & & H_{13}^+ & H_{12}^+ & H_{11} & \ddots \\ & & & \ddots & \ddots & \ddots \end{pmatrix}. \quad (\text{A5})$$

In the equation, each matrix element is not a pure number but a two-by-two matrix because it includes Pauli matrices. The elements  $H_{12}$  and  $H_{12}^+$  are the nearest hopping terms, and  $H_{13}$  and  $H_{13}^+$  stand for the next nearest hopping. Letting  $N = 2$  in Eq. (A4), we have

$$\begin{aligned} H_{11} &= U + [(M^2 + 1/2)\sigma_+ + \text{H.c.}], \\ H_{12} &= \sigma_z/2i + [M\sigma_+ + \text{H.c.}], \\ H_{13} &= \sigma_+/4 + \text{H.c.} \end{aligned} \quad (\text{A6})$$

The Hamiltonian matrix can be divided into blocks (each block is  $2 \times 2$ ) as shown in Eq. (A5) and can be viewed as a block tridiagonal matrix. The division strategy is not unique but is demonstrated in the equation as an example. If needed, the Hamiltonian can be split into blocks of dimension  $3 \times 3$

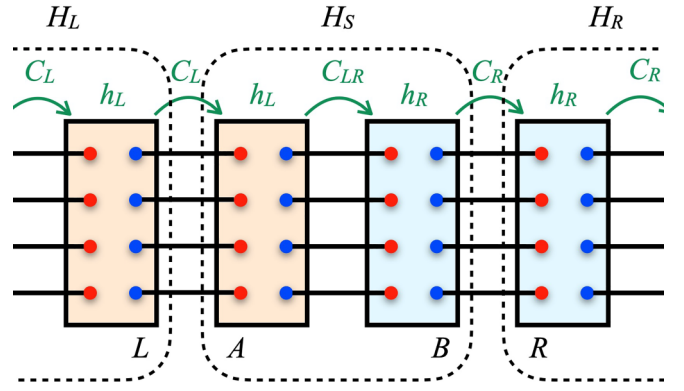


FIG. 6. The junction formed by joining two semiinfinite chains.

(Any choice of  $n \times n$  with  $n \geq 2$  is physically allowed). Because of the translational symmetry, the main diagonal blocks, the upper diagonal blocks, the lower diagonal blocks are respectively identical. The block Hamiltonian can be expressed more compact as

$$H = \begin{pmatrix} \ddots & \ddots & & & \\ \ddots & h & C & & \\ & C^+ & h & \ddots & \\ & & & \ddots & \ddots \end{pmatrix}, \quad (\text{A7})$$

with the block matrices

$$h = \begin{pmatrix} H_{11} & H_{12} \\ H_{12}^+ & H_{11} \end{pmatrix}, \quad C = \begin{pmatrix} H_{13} & 0 \\ H_{12} & H_{13} \end{pmatrix}. \quad (\text{A8})$$

The Hamiltonian describes an infinite 1D translational chain, of which  $h$  stands for the Hamiltonian of the extended translational cell and  $C$  means the adjacent coupling. In the Hamiltonian, we eliminate the non-nearest couplings at the cost of cell extension.

The junction system consists of two semi-infinite chain and the connection between them, as shown in Fig. 6. The regions of  $z < 0$  and  $z > 0$  are renamed by the left and right parts. The Hamiltonian of each semi-infinite chain can be obtained by truncating the matrix of the full infinite chain at the interface. For computational convenience, we adjust the division strategy in Eq. (A5) so that the size of left cells is identical to that of right cells. (In the calculation of main text, the  $3 \times 3$  strategy is adopted because  $N_1 = 3$  and  $N_2 = 2$ .) The jointing of the two semi-infinite chain provides the definition of the interface region, which is made up by the end cells of the left and right semi-infinite chains. The Hamiltonian of the interface region is

$$H_S = \begin{pmatrix} h_L & C_{LR} \\ C_{LR}^+ & h_R \end{pmatrix}, \quad (\text{A9})$$

where  $h_L$  and  $h_R$  are the cell Hamiltonians of left and right sides,  $C_{LR}$  is the coupling between the cells closest to the interface. The interface coupling is assumed to be the average of the intercell coupling in left side,  $C_L$ , and that in the right side,  $C_R$ .

## APPENDIX B: REFLECTION AND TRANSMISSION COEFFICIENTS IN TIGHT-BINDING METHOD

We divide the whole system into three parts (see Fig. 6), the left region, the scattering region, and the right region. The left and right regions have translational symmetry and the scattering only happens in the center region. For our junction system, the scattering region is defined same as the interface region, which only includes the right end cell of the left chain and the left end cell of the right chain.

Applying the Schrödinger equation  $H\psi = E\psi$  on the whole system, we have the local equation of the wave function in the scattering region

$$H_S\psi_S + H_{SL}\psi_L + H_{SR}\psi_R = E\psi_S, \quad (\text{B1})$$

where  $\psi_S$ ,  $\psi_L$  and  $\psi_R$  are the wave functions in the scattering region, the left side and right side respectively,  $H_S$  is the Hamiltonian of the scattering region, and  $H_{SL}$  ( $H_{SR}$ ) is the coupling Hamiltonian between the scattering region and the left (right) sides. By defining the isolated Green's function of the scattering region,  $G_S = (E - H_S)^{-1}$ , the above equation is reduced to

$$\psi_S = G_S H_{SL} \psi_L + G_S H_{SR} \psi_R. \quad (\text{B2})$$

The coupling Hamiltonian  $H_{SL}$  takes effect between the grids adjacent to left boundary of the scattering region. The grids of the scatter region are adjacent to left boundary are labeled by  $A$  and those in the left side are denoted by  $L$  (see Fig. 6). Similarly,  $H_{SR}$  works between the grids adjacent to right boundary, and we label the grids of the scatter region adjacent to the boundary by notation  $B$  and mark those in the right side by  $R$  (see Fig. 6). Applying the above equation not on the whole scattering region, but on grids  $A$  and  $B$ , we have

$$\begin{aligned} \psi_A &= G_{AS} H_{SL} \psi_L + G_{AS} H_{SR} \psi_R, \\ \psi_B &= G_{BS} H_{SL} \psi_L + G_{BS} H_{SR} \psi_R, \end{aligned} \quad (\text{B3})$$

where  $\psi_\alpha$  is the wave function on grids  $\alpha$  with  $\alpha = A, B$  and  $G_{\alpha S}$  means the block of grids  $\alpha$  cross the scattering region.

Considering an electron is injected from eigenmode  $|\phi^f\rangle_m$  of the left side, reflected to another eigenmode  $|\phi^b\rangle_n$  and transmitted to the eigen mode  $|\phi^f\rangle_{n'}$  of the other side, the above equation is

$$\begin{aligned} |\phi_A^f\rangle_m + \sum_n |\phi_A^b\rangle_n r_{nm} &= D_{AL} \left( |\phi_L^f\rangle_m + \sum_n |\phi_L^b\rangle_n r_{nm} \right) \\ &\quad + D_{AR} \sum_n |\phi_R^f\rangle_n t_{nm}, \\ \sum_n |\phi_B^f\rangle_n t_{nm} &= D_{BL} \left( |\phi_L^f\rangle_m + \sum_n |\phi_L^b\rangle_n r_{nm} \right) \\ &\quad + D_{BR} \sum_n |\phi_R^f\rangle_n t_{nm}, \end{aligned} \quad (\text{B4})$$

where  $r_{nm}$  and  $t_{nm}$  are the reflection and transmission coefficients from mode  $m$  to mode  $n$ ,  $|\phi_\alpha^f\rangle_m$  and  $|\phi_\alpha^b\rangle_m$  are the wave function of forward and backward modes  $m$  distributed on grids  $\alpha$  and  $D_{\alpha\beta} = G_{\alpha S} H_{S\beta}$  with  $\alpha, \beta = L, A, B, R$ . Because the equation holds for any incident mode, we place the eigen modes one by one to construct the matrices

$$\begin{aligned} \Phi_\alpha^f &= [|\phi_\alpha^f\rangle_1, |\phi_\alpha^f\rangle_2, \dots], \\ \Phi_\alpha^b &= [|\phi_\alpha^b\rangle_1, |\phi_\alpha^b\rangle_2, \dots], \end{aligned} \quad (\text{B5})$$

so as to the set of equations for all incident modes can be equivalent to one matrix equation. The matrix version of Eq. (B4) reads

$$\begin{aligned} \Phi_A^f + \Phi_A^b r &= D_{AL} (\Phi_L^f + \Phi_L^b r) + D_{AR} \Phi_R^f t, \\ \Phi_B^f t &= D_{BL} (\Phi_L^f + \Phi_L^b r) + D_{BR} \Phi_R^f t, \end{aligned} \quad (\text{B6})$$

where  $r$  and  $t$  are the reflection and transmission matrices with elements  $r_{nm}$  and  $t_{nm}$ , respectively. Rearrange the terms of two sides, the equation can be transform to

$$\begin{aligned} &\begin{pmatrix} \Phi_A^b - D_{AL} \Phi_L^b & -D_{AR} \Phi_R^f \\ -D_{BL} \Phi_L^b & \Phi_B^f - D_{BR} \Phi_R^f \end{pmatrix} \begin{pmatrix} r \\ t \end{pmatrix} \\ &= \begin{pmatrix} -\Phi_A^f + D_{AL} \Phi_L^f \\ D_{BL} \Phi_L^f \end{pmatrix}. \end{aligned}$$

After solving the equation, the reflection and transmission matrices are obtained. For the Hamiltonian in Eq. (1), only one propagating forward mode is allowed. We label the mode as the first one, so only the matrix element  $r_{11}$ , which is expressed as  $r$  in the main text, is needed to obtain the reflection shift.

## APPENDIX C: INTERFACE GREEN'S FUNCTION

To obtain the interface DOS, we have to calculate the interface Green's function  $G$  first. The interface Green's function is defined in the interface region and includes the effects induced by the semi-infinite chains besides. It is calculated by

$$G = (E - H_S - \Sigma_L - \Sigma_R)^{-1}, \quad (\text{C1})$$

where  $\Sigma_L$  and  $\Sigma_R$  are the self-energies of the left and right semi-infinite chains. By using the eigen modes obtained in Appendix B, the self-energies can be direct written down as

$$\begin{aligned} \Sigma_L &= C_L^+ \Phi_L^b (\Phi_A^b)^{-1}, \\ \Sigma_R &= C_R \Phi_R^f (\Phi_B^f)^{-1}. \end{aligned} \quad (\text{C2})$$

So we have the self-energies without iterative calculation and the interface Green's function can be obtained.

- [1] M. Onoda, S. Murakami, and N. Nagaosa, *Phys. Rev. Lett.* **93**, 083901 (2004).  
 [2] Z.-M. Yu, Y. Liu, and S. A. Yang, *Front. Phys.* **14**, 33402 (2019).  
 [3] G. Xu, H. Weng, Z. Wang, X. Dai, and Z. Fang, *Phys. Rev. Lett.* **107**, 186806 (2011).

- [4] A. A. Burkov and L. Balents, *Phys. Rev. Lett.* **107**, 127205 (2011).  
 [5] L. Lu, Z. Wang, D. Ye, L. Ran, L. Fu, J. D. Joannopoulos, and M. Soljačić, *Science* **349**, 622 (2015).

- [6] J. Xiong, S. K. Kushwaha, T. Liang, J. W. Krizan, M. Hirschberger, W. Wang, R. J. Cava, and N. P. Ong, *Science* **350**, 413 (2015).
- [7] C.-L. Zhang, S.-Y. Xu, I. Belopolski, Z. Yuan, Z. Lin, B. Tong, G. Bian, N. Alidoust, C.-C. Lee, S.-M. Huang, T.-R. Chang, G. Chang, C.-H. Hsu, H.-T. Jeng, M. Neupane, D. S. Sanchez, H. Zheng, J. Wang, H. Lin, C. Zhang *et al.*, *Nat. Commun.* **7**, 10735 (2016).
- [8] N. P. Armitage, E. J. Mele, and A. Vishwanath, *Rev. Mod. Phys.* **90**, 015001 (2018).
- [9] A. Burkov, *Annu. Rev. Condens. Matter Phys.* **9**, 359 (2018).
- [10] B. Q. Lv, T. Qian, and H. Ding, *Rev. Mod. Phys.* **93**, 025002 (2021).
- [11] A. Ahmad and G. Sharma, *Phys. Rev. B* **103**, 115146 (2021).
- [12] H. Li, H. Liu, H. Jiang, and X.-C. Xie, *Phys. Rev. Lett.* **125**, 036602 (2020).
- [13] A. C. Potter, I. Kimchi, and A. Vishwanath, *Nat. Commun.* **5**, 5161 (2014).
- [14] Y. Araki, A. Yoshida, and K. Nomura, *Phys. Rev. B* **94**, 115312 (2016).
- [15] H. Ishida and A. Liebsch, *Phys. Rev. B* **98**, 195426 (2018).
- [16] V. Dwivedi, *Phys. Rev. B* **97**, 064201 (2018).
- [17] G. Murthy, H. A. Fertig, and E. Shimshoni, *Phys. Rev. Res.* **2**, 013367 (2020).
- [18] F. Abdulla, S. Rao, and G. Murthy, *Phys. Rev. B* **103**, 235308 (2021).
- [19] S. Kaushik, I. Robredo, N. Mathur, L. M. Schoop, S. Jin, M. G. Vergniory, and J. Cano, *arXiv:2207.14109*.
- [20] F. Bucccheri, R. Egger, and A. De Martino, *Phys. Rev. B* **106**, 045413 (2022).
- [21] F. Bonasera, S.-B. Zhang, L. Privitera, and F. M. D. Pellegrino, *Phys. Rev. B* **106**, 195115 (2022).
- [22] N. Mathur, F. Yuan, G. Cheng, S. Kaushik, I. Robredo, M. G. Vergniory *et al.*, *Nano Lett.* **23**, 2695 (2023).
- [23] C. Fang, M. J. Gilbert, X. Dai, and B. A. Bernevig, *Phys. Rev. Lett.* **108**, 266802 (2012).
- [24] Q. Liu and A. Zunger, *Phys. Rev. X* **7**, 021019 (2017).
- [25] S.-M. Huang, S.-Y. Xu, I. Belopolski, C.-C. Lee, G. Chang, T.-R. Chang *et al.*, *Proc. Natl. Acad. Sci. USA* **113**, 1180 (2016).
- [26] B. Singh, G. Chang, T.-R. Chang, S.-M. Huang, C. Su, M.-C. Lin, H. Lin, and A. Bansil, *Sci. Rep.* **8**, 10540 (2018).
- [27] N. B. M. Schröter, S. Stolz, K. Manna, F. de Juan, M. G. Vergniory, J. A. Krieger *et al.*, *Science* **369**, 179 (2020).
- [28] T. Dubček, C. J. Kennedy, L. Lu, W. Ketterle, M. Soljačić, and H. Buljan, *Phys. Rev. Lett.* **114**, 225301 (2015).
- [29] Q. Lin, M. Xiao, L. Yuan, and S. Fan, *Nat. Commun.* **7**, 13731 (2016).
- [30] J. Noh, S. Huang, D. Leykam, Y. D. Chong, K. P. Chen, and M. C. Rechtsman, *Nat. Phys.* **13**, 611 (2017).
- [31] W. Song, S. Wu, C. Chen, Y. Chen, C. Huang, L. Yuan, S. Zhu, and T. Li, *Phys. Rev. Lett.* **130**, 043803 (2023).
- [32] N. Han, J. Liu, Y. Gao, K. Zhou, and S. Liu, *New J. Phys.* **24**, 053052 (2022).
- [33] E. Lustig and M. Segev, *Adv. Opt. Photon.* **13**, 426 (2021).
- [34] H. Ge, X. Ni, Y. Tian, S. K. Gupta, M.-H. Lu, X. Lin, W.-D. Huang, C. T. Chan, and Y.-F. Chen, *Phys. Rev. Appl.* **10**, 014017 (2018).
- [35] V. Peri, M. Serra-Garcia, R. Ilan, and S. D. Huber, *Nat. Phys.* **15**, 357 (2019).
- [36] C. W. J. Beenakker, R. A. Sepkhanov, A. R. Akhmerov, and J. Tworzydło, *Phys. Rev. Lett.* **102**, 146804 (2009).
- [37] S. A. Yang, H. Pan, and F. Zhang, *Phys. Rev. Lett.* **115**, 156603 (2015).
- [38] Q.-D. Jiang, H. Jiang, H. Liu, Q.-F. Sun, and X. C. Xie, *Phys. Rev. Lett.* **115**, 156602 (2015).
- [39] Y.-R. Hao, L. Wang, and D.-X. Yao, *Phys. Rev. B* **99**, 165406 (2019).
- [40] L. Wang and S.-K. Jian, *Phys. Rev. B* **96**, 115448 (2017).
- [41] Y. Liu, Z.-M. Yu, and S. A. Yang, *Phys. Rev. B* **96**, 121101(R) (2017).
- [42] L.-K. Shi and J. C. W. Song, *Phys. Rev. B* **100**, 201405(R) (2019).
- [43] R. Li, C.-X. Cui, X.-X. Zhou, and Z.-M. Yu, *Phys. Rev. B* **108**, 075149 (2023).
- [44] U. Chattopadhyay, L.-K. Shi, B. Zhang, J. C. W. Song, and Y. D. Chong, *Phys. Rev. Lett.* **122**, 066602 (2019).
- [45] M. Yang, H.-Y. Li, and R.-Q. Wang, *New J. Phys.* **23**, 113024 (2021).
- [46] M. Yang, Q.-T. Hou, and R.-Q. Wang, *New J. Phys.* **22**, 033015 (2020).
- [47] Y. Liu, Z.-M. Yu, C. Xiao, and S. A. Yang, *Phys. Rev. Lett.* **125**, 076801 (2020).
- [48] Q. Wang, M. Xiao, H. Liu, S. Zhu, and C. T. Chan, *Phys. Rev. X* **7**, 031032 (2017).
- [49] X. Fan, C. Qiu, Y. Shen, H. He, M. Xiao, M. Ke, and Z. Liu, *Phys. Rev. Lett.* **122**, 136802 (2019).
- [50] Z. Wang, Z. Wang, H. Li, J. Luo, X. Wang, Z. Liu, and H. Yang, *Appl. Phys. Express* **14**, 077002 (2021).
- [51] H. Zhang, S. Zhang, J. Liu, and B. Liu, *Appl. Sci.* **12**, 167 (2021).
- [52] See Supplemental Material at <http://link.aps.org/supplemental/10.1103/PhysRevB.109.035434> for the evolution of the reflection shift and interface DOS when the transmissive pocket position and size are varying.